

# Synthetic edge and SOL diagnostics – a bridge between experiments and theory

A. H. Nielsen<sup>1</sup>, O. Asztalos<sup>2</sup>, J. Olsen<sup>1</sup>, V. Naulin<sup>1</sup>, J. Juul Rasmussen<sup>1</sup>, A.S. Thrysøe<sup>1</sup>, T. Eich<sup>3</sup>, G.I. Pokol<sup>2,6</sup>, N. Vianello<sup>4</sup>, R. Coelho<sup>5</sup>, D.I. Refy<sup>6</sup>, B. Tal<sup>6</sup>, A. Buzas<sup>6</sup>, G.H. Hu<sup>7</sup>, N. Yan<sup>7</sup>, EUROfusion MST1 Team<sup>8</sup>, EUROfusion-IM Team<sup>9</sup> and ASDEX Upgrade Team<sup>10</sup>

<sup>1</sup> Department of Physics, Technical University of Denmark, Kgs. Lyngby, Denmark

<sup>2</sup> Institute of Nuclear Technique, Budapest University of Technology and Economics  
Budapest, Hungary

<sup>3</sup> Max-Planck Institute for Plasma Physics, Garching, Germany

<sup>4</sup> Consorzio RFX, Associazione EURATOM-ENEA sulla Fusione, Padova, Italy

<sup>5</sup> Instituto de Plasmas e Fusão Nuclear, Instituto Superior Técnico, Universidade de Lisboa  
Lisboa, Portugal

<sup>6</sup> Wigner Research Center for Physics, Budapest, Hungary

<sup>7</sup> Institute of Plasma Physics, Chinese Academy of Science, Hefei, Peoples Republic of China

<sup>8</sup> See the author list of H. Meyer et al., Nucl. Fusion 57, 102014 (2017)

<sup>9</sup> <http://euro-fusionscipub.org/eu-im>

<sup>10</sup> Max-Planck-Institut für Plasmaphysik, Boltzmannstrasse 2, D-85748 Garching, Germany

E-mail: ahnie@fysik.dtu.dk

Received xxxxxx

Accepted for publication xxxxxx

Published xxxxxx

## Abstract

The Scrape off Layer (SOL) plasma in a Tokamak device and its coupling with the edge dictate the performance of a discharge to a high degree – especially as all plasma has to go through the SOL, which is the main exhaust channel for the hot plasma. This contribution provides an introduction to the modelling efforts of the plasma dynamics in the SOL and the edge regions. We employ a fully dynamical fluid model, the HESEL code. HESEL is equipped with synthetic diagnostic tools as probe arrays, Li-beam spectroscopy, and Gas Puff Imaging. Using the synthetic probe arrays to measure the electron and ion heat advection and conduction we obtain the upstream power fall-off length for a broad range of plasma parameters and by applying non-linear fitting procedures we derive the scaling of the fall-off length. The obtained results are in agreement with recent experimental observations from L-mode ASDEX Upgrade data. A workflow for generating synthetic Lithium beam data, where the fluctuation data from HESEL are passed to the RENATE code are discussed using experimental results from ASDEX Upgrade.

Keywords: fusion, interchange dynamics, scrape-off-layer, turbulence, transport, synthetic diagnostics

---

## Introduction

The understanding of the Scrape off Layer (SOL) plasma is a key topic in contemporary fusion research. Any predictive capability for the design and operation of present and future fusion experiments – and of future fusion power plants – rely on that understanding. The SOL is a region, where both perpendicular and parallel transport are important. The plasma transport through the SOL is dominated by turbulent intermittent fluctuations organized into filamentary structures convecting particles, energy and momentum, see e.g. [1]. This highly intermittent transport cannot be described or parametrized by diffusion-convection type models, see [2][3]. To properly model the SOL dynamics it has become obvious in the last years that it is necessary to account for the full dynamical evolution of the SOL, treating the profile evolution on the same footing as the fluctuations.

For developing an insight into the dynamics of the SOL, it is necessary to have a coherent view on both SOL and edge and to combine advanced and detailed experimental investigations with modelling capable of resolving the complex dynamics of the coupled edge/SOL region, see [4][5][6][7][8]. Steady-state mean field models, despite detailed account of magnetic field geometry and the atomic physics issues, alone cannot develop this insight. By design, these models lack the intermittent dynamics of the edge/SOL plasma.

The strong and direct linking of experimental and modelling activities, especially synthetic diagnostics is essential for approaching full understanding and predictive capabilities of the SOL transport.

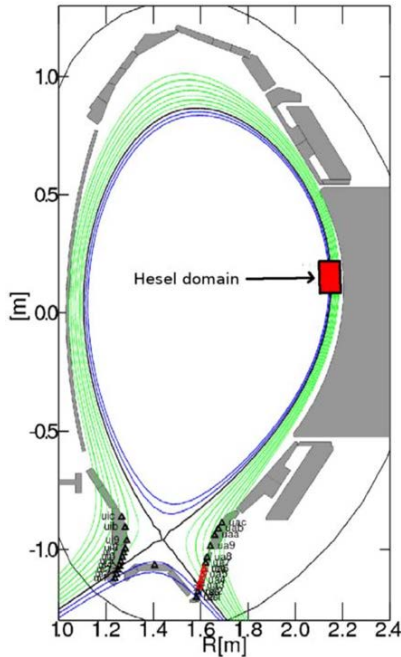


Figure 1 the cross-section of AUG with the HESEL domain indicated to scale by the red box.

To generate the synthetic diagnostic data we employ the 2D fluid model, HESEL, an energy-conserving, four-field model based on the Braginskii equations [9] governing the dynamics of a quasi-neutral, simple plasma. For a detailed description of the numerical model and code, see [4][10]. It describes interchange-driven, low-frequency turbulence in a plane perpendicular to the magnetic field at the outboard midplane. In the limit of constant ion pressure the model reduces to the ESEL (edge-sol-electrostatic) model, which has successfully modelled fluctuations and profiles for a number of tokamaks; JET[11], MAST[12], EAST[13], ASDEX Upgrade [14] and TCV[15]. The code simulates density, ion and electron pressure evolution together with the evolution of the generalized vorticity. It assumes that the SOL is mainly fueled at the outboard midplane due to radial transport of heat and particles caused by interchange-driven, low-frequency turbulence. Parallel losses, including sheath couplings at the material surfaces, have been parameterized in the SOL.

Figure 1 shows a cross-section of ASDEX Upgrade (AUG) and with the HESEL domain inserted on the outboard midplane. In Figure 2, we show the HESEL domain in detail with the closed field line region, the edge region including the inner part, where prescribed experimental profiles are active, and the open field line region, the SOL. For comparison with experiments, HESEL is equipped with synthetic diagnostic tools such as probe arrays, Li-beam spectroscopy, and Gas Puff Imaging. These diagnostics have been developed within the EUROfusion Integrated Modelling framework (EU-IM) [16][17].

Experimentally probes have been used extensively in the SOL on a wide range of different tokamaks, see e.g. [18][19][13][12]. Characteristics for these measurements are that the probability density function of, e.g., ion saturation current is asymmetric and skewed and can mostly be well approximated by a Gamma distribution, see e.g. [20][21][22]. This distribution results from that the density in the SOL can be considered as made up by non-interacting and randomly occurring pulses, see [23][24][25]. Analysing both synthetic and experimental beam emission spectroscopy lithium beam signals using AUG data we show that these signals have the same statistical properties as probe signals.

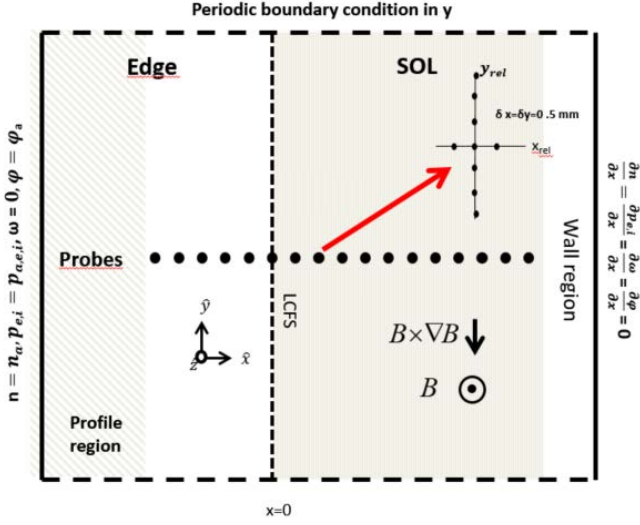


Figure 2 The HESEL domain showing the closed field line region, the edge, and the open field line region, the SOL. Prescribed profiles are only active in the inner half of the edge region. The insert shows the probe setup.

## SYNTHETIC DIAGNOSTICS

As input for our simulations, we apply data from experiments on AUG, where filamentary transport was investigated and these studies were part of plasma operations

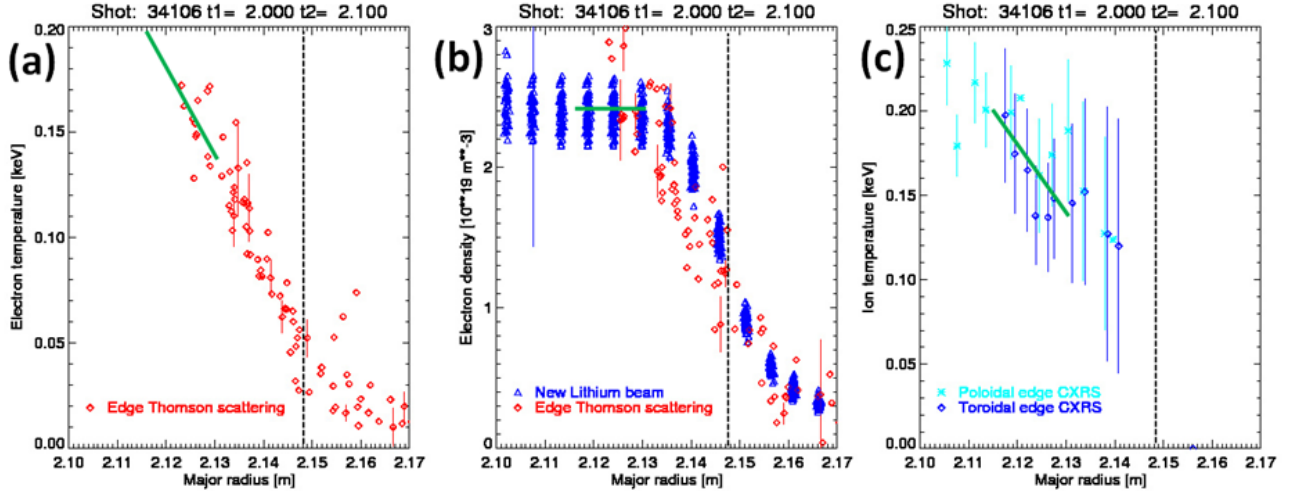


Figure 3 Output from AUGPED for the AUG discharge #34106 at Time=2s-2.1s showing the edge/SOL profiles of (a) electron temperature, (b) electron density and (c) ion temperature. The added full green lines denote the forcing profiles used in the inner half of the edge region in HESEL. Vertical black dotted lines denote the position of the LCFS, corresponding to  $x=0$  in the HESEL model, see Figure 2.

### 1.1. Synthetic Langmuir probes

The HESEL code has previously been applied to investigate the radial transport of poloidal momentum for AUG in L-mode. In that project we simulated the setup of the Stuttgart probe and generated synthetic ion saturation currents and floating potentials, taking into account the relative radial and poloidal positions of the individual pins,

within the EUROfusion work program on Medium-Size Tokamak Campaigns. In this section, we investigate discharge #34106, which is a L-mode with deuterium plasma, operated in Lower Single Null configuration. Energy input consisted of 0.7 MW of Ohmic power and 0.55 MW of NBI. Figure 3 shows the experimentally obtained pedestal profiles of electron density and electron and ion temperature, respectively, from the edge Thomson scattering, the New Lithium beam and the poloidal and toroidal edge CXRS diagnostics. In solid green are plotted fitted edge profiles, used in HESEL as forcing profiles, see profile region in Figure 2. We have performed a HESEL simulation, HESEL@AUG#34106, using these profiles and parameters; major radius  $R=1.65$  m, minor radius  $a=0.5$  m, the magnetic field on axis  $B_0=2.92$  T, safety factor  $q_{95}=3.95$ . To calculate the neo-classical dissipation coefficients in the model, we use characteristic parameters at the last closed flux surface (LCFS) at  $R_{\text{sep}}=2.1475$  m, as denoted by the vertical black dotted lines in Figure 3; electron density  $n_{e,0}=1.5 \times 10^{19} \text{ m}^{-3}$ , electron temperature  $T_{e,0}=50$  eV, and ion temperature  $T_{i,0}=75$  eV. In the next sections, we will use the results from this simulation to investigate radial and parallel transport.

see [26]. Due to the absence of a high sampled electron temperature, information about the radial momentum transport was shown to be difficult to obtain.

Also, the three-dimensional gyrofluid delta-f model GEMR code has been used to generate synthetic probe signals, see [27][28]. The ESEL code, i.e. HESEL without ion dynamics and sheath connection in SOL, has previously been used to investigate synthetic probes for L-mode

discharges in the colder SOL of MAST, see [12]. In these cases, tendencies similar to those reported here were observed, namely that electron temperature and especially its fluctuations must be taken into account to evaluate probe data.

In this section, we will focus on the radial velocity and the radial particle transport, essential quantities regularly being derived from Langmuir probe measurements. Here, we have aligned the individual pins in a regular grid aligned along the radial-poloidal coordinates; see Figure 2. We investigate the measurement of the transport for the case, where the temporal electron and ion temperature signals are absent and we only have information about their time average values,  $\langle T_e \rangle$  and  $\langle T_i \rangle$ . Also, we investigate the influence of poloidally separated pins for measuring the radial ExB drift velocity.

Numerically, we have access to signals with high spatial and temporal resolution, and we can readily generate synthetic signals. The individual pins of the probes in Figure 2 measure all relevant plasma fields with a sampling rate of 10 MHz. We note that experimentally, we are limited by that 1 pin measures only a single field.

In Figure 4, we display the density, electron and ion temperatures at three different times from HESEL@AUG#34106. A plasma filament ejected from the edge region into the SOL is seen in all three fields.

In Figure 5 we display the temporal signals from the synthetic probe positioned at the radial position  $x=10$  mm with respect to the LCFS position, i.e., in the SOL. The individual frames display both ‘raw’ HESEL signals in SI unit and signals derived from the synthetic probes. 5 events are clearly visible in all the subfigures corresponding to a frequency of filaments of approximately 5kHz. This frequency is consistent with frequencies of filaments in SOL observed experimentally in medium size tokamaks in L-mode, see e.g. [21][27].

Figure 5(a) displays the electron density,  $n_e$ , and the signal  $n_{e,sat} = I_{sat}/eA\sqrt{(\langle T_e \rangle + \langle T_i \rangle)/m_i}$ , where  $I_{sat} = n_e e A C_s$  is the ion saturation current,  $A$  is the area of the probe and  $C_s = \sqrt{(T_e + T_i)/m_i}$  is the ion sound speed. Overall, we see that the two signals are closely correlated with their average approximately the same, but during the

intermittent fluctuations  $n_{e,sat}$  is significantly larger than the true electron density.

Figure 5(b) displays the electron and ion temperature fluctuations. The electron temperature is significantly smaller than the ion temperature, a result of the strong parallel heat conduction present in the SOL, but both signals have strong similar fluctuations, and these are correlated with the electron density fluctuations.

Figure 5(c) displays the plasma potential,  $\phi_p$ , and floating potentials,  $\phi_f = \phi_p - \alpha T_e/e$ , where  $\alpha=3.18$  for a deuterium plasma. We observed large differences between the two signals, not only in absolute values, but also in frequencies. The plasma potential is slowly varying with a high mean value, whereas the floating potential exhibits much faster variations similar to the electron temperature and a mean value around zero.

Figure 5(d) displays the ExB radial drift velocity,  $V_r$ , and the velocities calculated from the potential difference of two Langmuir pins separated poloidally by  $dy = 5$  mm using plasma potential;  $V_r^p = (\phi_p^1 - \phi_p^2)/dy$  and using floating potential;  $V_r^f = (\phi_f^1 - \phi_f^2)/dy$ . For the last field, we observe different amplitudes and the fluctuations seem to be nearly 90 degrees out of phase compared to the other two signals. The electron temperature fluctuations are large in the SOL and they will dominate the floating potential.  $V_r^f$  will, in this case, be proportional to the negative gradient of the electron temperature. We, therefore, conclude that velocity based on floating potential cannot be taken as a proxy for the true ExB drift velocities at these SOL temperatures. Moving inward towards the edge region the electron temperature will increase, driving the signals even further apart.

In Figure 5(e) we present 3 different estimates of the radial particle flux;  $\Gamma_n = n_e V_r$ ,  $\Gamma_n^p = n_e V_r^p$  and  $\Gamma_n^f = n_e V_r^f$ , where the radial velocities are taken from the above frame. Evaluating the temporal mean values using the full time span of the particle fluxes we obtain;  $\langle \Gamma_n \rangle = 3.6 \times 10^{20} \text{m}^{-2} \text{s}^{-1}$ ,  $\langle \Gamma_n^p \rangle = 2.9 \times 10^{20} \text{m}^{-2} \text{s}^{-1}$  and  $\langle \Gamma_n^f \rangle = -4.84 \times 10^{20} \text{m}^{-2} \text{s}^{-1}$ . As the averaged flux derived using the floating potential is negative, whereas the two other signals are positive, we infer that we cannot reproduce the radial velocity using this potential.

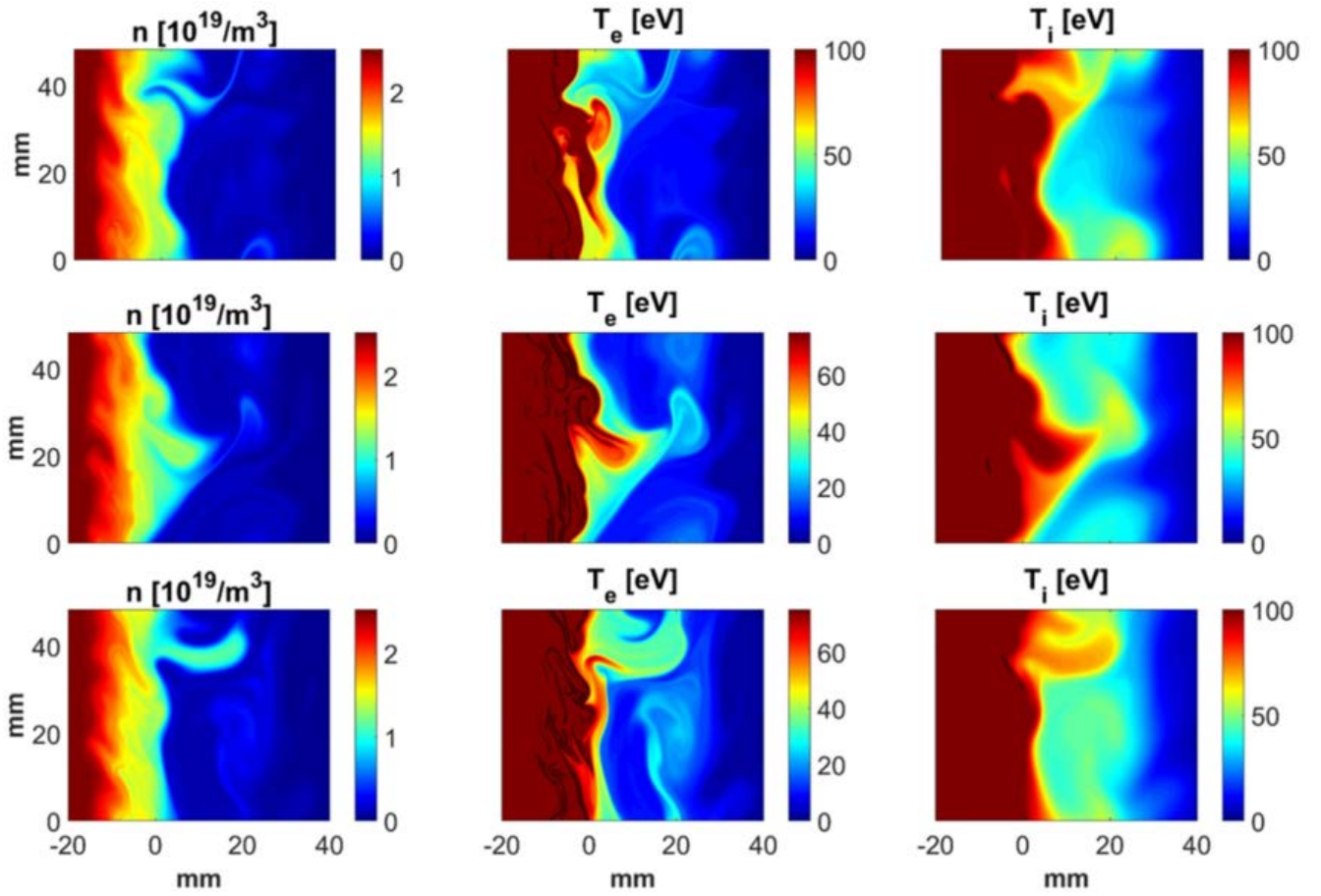


Figure 4 For HESEL@AUG#34106 snapshots of the electron density, electron temperature and ion temperature for three different times, top row:  $t=0.4065$  ms, middle row: time=0.4175 ms and bottom row:  $t=0.4282$  ms



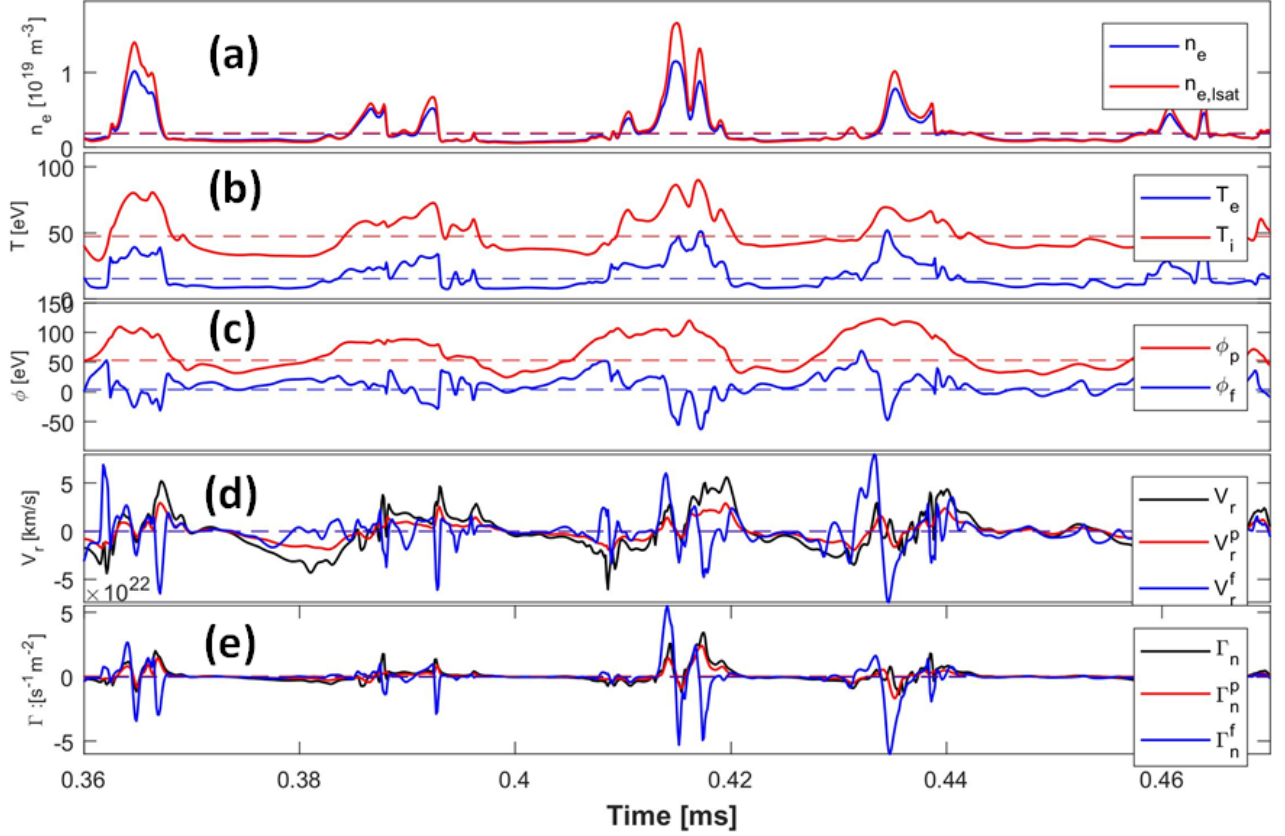


Figure 5 Temporal evolution of signals obtained by the synthetic probe positioned at the radial position at  $x=10$  mm in the SOL from the simulation in Figure 4. (a) The electron density variation,  $n_e$ , and density derived from the ion saturation current for constant electron temperature,  $n_{e,lsat}$ , (b) the electron and ion temperatures,  $T_e$  and  $T_i$ , (c) the plasma and floating potentials,  $\phi_p$  and  $\phi_f$ , (d) the true radial velocity,  $V_r$ , and velocities based on plasma potential difference from two probes separated poloidally by 5 mm; plasma potential  $V_r^p$  and floating potential  $V_r^f$ , and (e) the true particle flux,  $\Gamma_n$ , and particle flux based on plasma and floating potential differences  $\Gamma_n^p$  and  $\Gamma_n^f$ . Horizontal dashed lines in (a), (b) and (c) denote the average values of the respective signals.

To investigate the effect of pin separation for the determination of the ExB drift velocity in more detail, we display in Figure 6 the temporal evolution of radial velocity for  $x=10$  mm using 4 different poloidal pin separations. Choosing the largest pin separation we will reproduce a signal somewhat similar to the true ExB drift velocity, especially concerning the temporal frequencies present in the signal, but we do obtain a significantly smaller signal. We cannot obtain contributions from spatial variations smaller than the separation. Filament sizes for this simulation are in the range of 10-15 mm and we observed that we need a pin separation no larger than 5 mm to obtain a velocity close to the true drift velocity. In Figure 7, we present the radial profile of the particle flux for the same pin separations as in Figure 6. We notice large fluctuations in the signals, which are due to the finite time record. Flux events are very intermittent in both time and space and we need a large record to obtain a reliable average. We observed that there is an increase in radial particle flux around  $x=20$  mm, which is a result of only 2-3 large transport events reaching this part of the SOL. In the edge region, e.g.  $x<0.0$  mm, we again

observed smaller measured flux as pin separation increases, consistent with the results for the drift velocity in Figure 6.

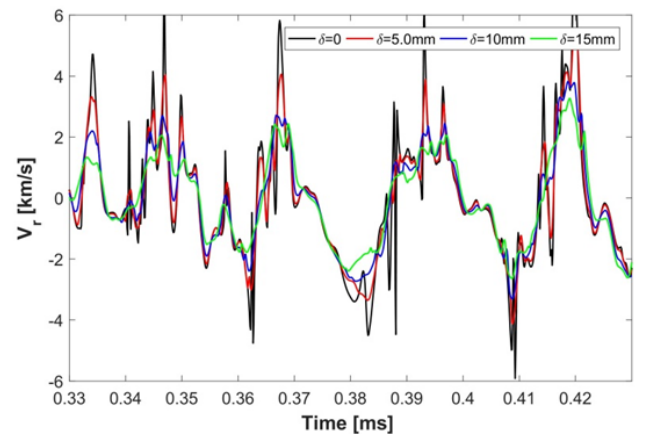


Figure 6 The time evolution of the radial velocity,  $V_r^\delta$ , measured by the plasma potential separated poloidally by 0, 5, 10 and 15 mm for a radial position of  $x=10$  mm.

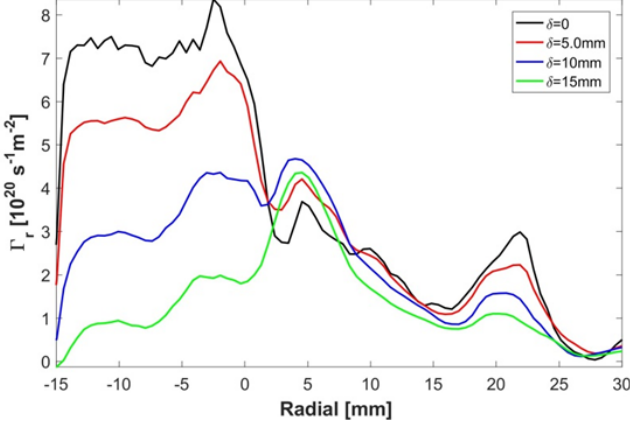


Figure 7 The radial profiles of the particle flux,  $\Gamma_r^\delta = \langle n_e V_r^\delta \rangle$ , averaged over 1.4 ms, where the same pin separation Figure 6 has been used.

## 1.2. Parallel transport

To evaluate the power fall-off length on the outboard midplane we need a large number of radially separated synthetic probes as the power fall-off length is only some millimetres thick. For these AUG simulations, we have probes separated by a radial distance of just 0.5 mm, approximately the gyroradius of the ions but still 10 larger than the resolution of the numerical grid. Additionally, we also need a time record sufficiently large to capture a large number of events, i.e. blobs and filaments, as parallel transport is highly intermittent.

Figure 8 displays the time evolution of the parallel electron heat conduction density,  $q_{||,SH,e}(t) = a \frac{P_e}{\tau_{SH,e}} \tau_{SH,e}$  being the loss rate of the electron Spitzer-Härm conduction, see [13], for two radial positions: at the LCFS and for  $x=10$  mm. We observe that for both positions the signals are very intermittent and we can observe transport events more than 5 times larger than the mean value. We note that as  $q_{||,SH,e} \propto T_e^{7/2}$  most of the heat in the electron channel will be lost very close to the LCFS, explaining the large difference in amplitude of  $q_{||,SH,e}$  between Figure 8(a) and Figure 8(b). Also, we will obtain a significant smaller parallel heat transport if we use the mean value of  $T_e$  instead of the full temporal signal. For the simulations shown in this paper we obtain;  $q_{||,SH,e}(T_e) \sim 2q_{||,SH,e}(\langle T_e \rangle)$  see also [14].

Figure 9 displays the radial profile of parallel heat transport, i.e. by averages of signals like the one shown in Figure 8. We refer to [13] for details of obtaining these profiles. The parallel heat flux is divided into 3 contributions; electron conduction  $P_{q||,SH,e} = 2\pi(R+a) \int_0^\infty q_{||,SH,e} dx = 0.329$  MW, where  $2\pi(R+a)$  factor accounts for the circumference of the tokamak, electron

advection  $P_{q||,a,e} = 0.161$  MW and finally ion advection  $P_{q||,a,i} = 0.301$  MW, where the parallel electron and ion heat advection are given as:  $q_{||,a,\alpha}(t) = a \frac{P_\alpha}{\tau_d}$ ,  $\alpha = \{e, i\}$ , see [13] for details. We point out that the ion conduction is negligible for the present case. The total power across the LCFS is  $P = P_{q||,SH,e} + P_{q||,a,e} + P_{q||,a,i} = 0.791$  MW. Taking the ‘simplicity’ of the model into account, this is fairly close to the actual heating power used  $P_{NBI} + P_{Ohmic} = 1.25$  MW.

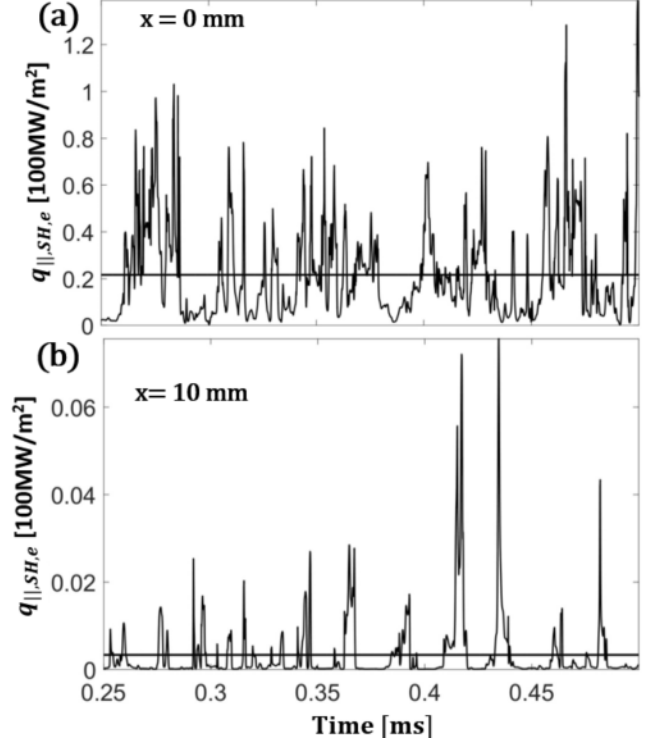


Figure 8 Temporal variations of the parallel electron heat conduction density for two radial positions in the SOL Horizontal line denote the time average.

In Figure 10, we have plotted the power law for the power fall-off length,  $\lambda_q$ , for a number of HESEL simulations with AUG parameters, see [13]. We have included further HESEL@AUG simulations; #34106, #31344, #29302 and #29308 to illustrate that they follow the HESEL@AUG power law derived in [13]. Our HESEL@AUG simulations are also in agreement with experimental L-mode Sieglin scaling at AUG, see [27];

$$\lambda_{q,Sieglin}(\text{mm}) = (1.45 \pm 0.13) P^{-0.14 \pm 0.05} q^{1.07 \pm 0.07} B^{-0.78}$$

$$\lambda_{q,Olsen}(\text{mm}) = (1.71 \pm 0.28) P^{-0.16 \pm 0.04} q^{0.84 \pm 0.05} B^{-0.31 \pm 0.20}$$

where the Olsen scaling,  $\lambda_{q,Olsen}$  [14], is the power law derived from a series of HESEL@ASDEX turbulence simulations. In both scalings, there is only a weak variation due to the input power,  $P$ , on  $\lambda_q$  and a nearly linear variation on safety factor  $q$ . Note that for the Sieglin scaling the magnetic field variation are taken from H-mode experiments.

In Figure 11 we display the power law for the power fall-off length,  $\lambda_q$ , for all the simulations presented in Figure 10, but now only using the safety factor,  $q$ , and the ion pressure gradient across the LCFS,  $|\nabla P_{i,LCFS}|$ , for the fit. We observe a fit

$$\lambda_q(\text{mm}) = (1.55 \pm 0.12) q^{0.51 \pm 0.05} |\nabla P_{i,LCFS}|^{-0.26 \pm 0.03}$$

with a coefficient of determination of  $R^2 = 0.95$ , which is the highest coefficient we have obtained for this set of simulations. The motivation for using the ion pressure gradient is that the turbulence is created due to interchange dynamics, i.e., pressure gradients, in the edge region and resulting in filaments transporting plasma into the SOL. Due to the correlation between ion and electron pressures we obtain practically the same fit using electron pressure gradients instead of ion pressure gradients, but with a slightly lower coefficient of determination.

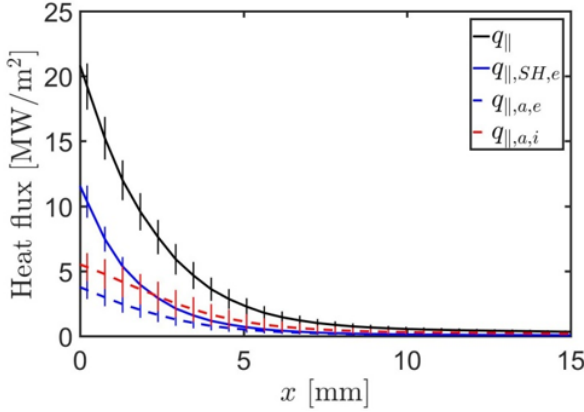


Figure 9 Radial profiles of parallel electron heat conduction density (blue), parallel electron heat advection (dashed blue), the parallel ion heat advection (dashed red) and the total parallel heat transport (black) derived from the synthetic probes.

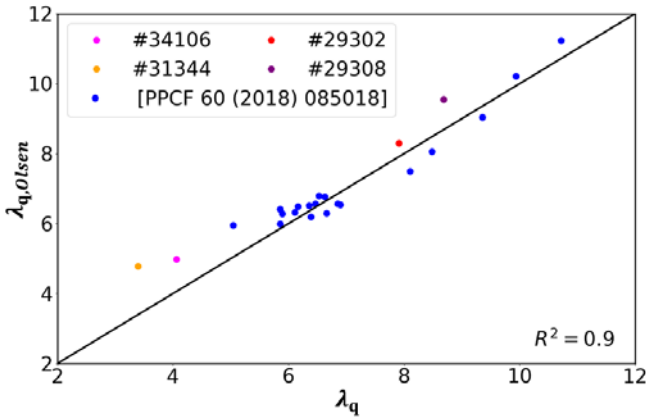


Figure 10 The power fall-off length obtained from the Olsen AUG scaling,  $\lambda_{q,Olsen} = 1.71 P^{-0.16} q^{0.84} B^{-0.31}$  plotted against the measured power fall-off length,  $\lambda_q$ , for the HESEL@AUG simulations presented in [13], the blue dots. Also plotted are the

HESEL@AUG#34106 simulation (integration of the black curve in Figure 9) and three other HESEL@AUG L-mode simulations.

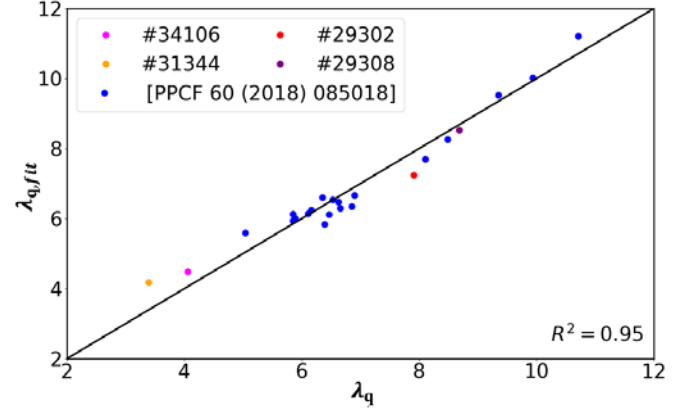


Figure 11 The power fall-off length obtained from  $\lambda_{q,fit} = 1.55 q^{0.51} |\nabla P_{i,LCFS}|^{-0.26}$  plotted against the measured power fall-off length,  $\lambda_q$ .  $\lambda_{q,fit}$  has been derived using all the HESEL@ASDEX simulations presented in Figure 10.



## Synthetic lithium beam diagnostics

Beam emission spectroscopy (BES) is an important plasma diagnostic for the measurement of plasma density and related fluctuations [28], by the observation of spontaneous emission from a high energy atomic beam injected into the plasma. The atomic beam typically consists of hydrogen species or light alkali atoms, which suffer collisional excitations and de-excitations with plasma particles, while gradually attenuating due to ionization and charge exchange processes. Rate Equations for Neutral Alkali-beam Technique (RENATE) is a BES modelling code, which calculates the electron population evolution of atomic levels along the beam for arbitrary density and temperature profiles [31]. The code features 3D beam and observation geometry modelling within measured magnetic geometries accounting for all BES related spatial artefacts. A SOL synthetic diagnostic developed by means of coupling the RENATE and HESEL codes required the 2D slab geometry used by the latter to be extended into 3D and placed within the machine coordinate space to the required position of the LCFS.

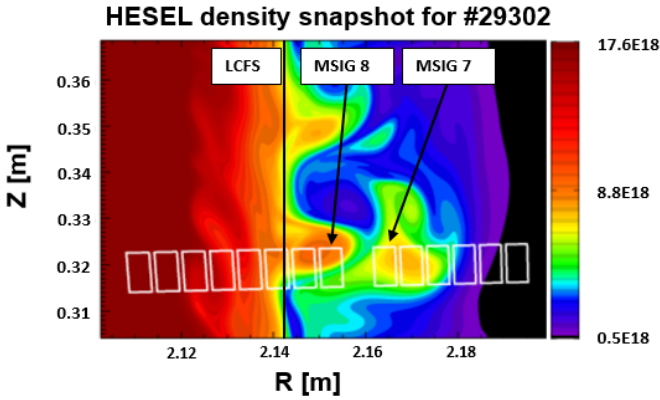


Figure 12: HESEL density snapshot based on AUG discharge 29302@3s, a poloidal projection of modelled LiBES observation geometry marked with white boxes. LCFS is located at  $R=2.145$  m. The Inner SOL channels 'MSIG-7' and 'MSIG-8' are pointed out.

Plasma parameters are assumed to be constant along field lines, due to the sampling time of the BES system exceeding that of the time of flight of particles following magnetic field lines within the beam geometry.

Figure 12 shows the poloidal projection of the ASDEX lithium BES observation geometry [32] on a HESEL density snapshot positioned in the path of the diagnostic beam. Detector channels MSIG-7 and MSIG-8 are pointed out. Due to the limitation of the RENATE the observation fibres were approximated with rectangular detector pixels, which projected onto the beam have a similar radial distribution and poloidally elongated to have the same collection surface as the diagnostic. A 200 kHz temporal and 0.5-1 cm optical resolution which increases to 2 –3 cm due to atomic physics

processes. The diagnostic has a reasonable 1-10 signal to noise ratio allows for a detailed study of SOL turbulence, as shown in previous works [33]. The RENATE-HESEL synthetic diagnostic is a new tool in the study of SOL turbulence and we aim at comparing our results with experimental observations. AUG discharge #29302 was selected, which contains a 0.5 – 0.6 s time window of steady-state L-mode operations and is featured was used in Birkenmeier *et al* [33].

The general parameters for this discharge taken for the HESEL modelling are as follows:  $R=1.65$  m,  $a=0.5$  m,  $B_0 = 2.5$  T,  $q_{95}=6.85$ ,  $n_{e,0} = 1.3 \times 10^{19} \text{ m}^{-3}$ ,  $T_{e,0} = 50$  eV and  $T_{i,0} = 75$  eV. Profiles from the electron density and temperatures are, as in Figure 3, taken from AUGPED.

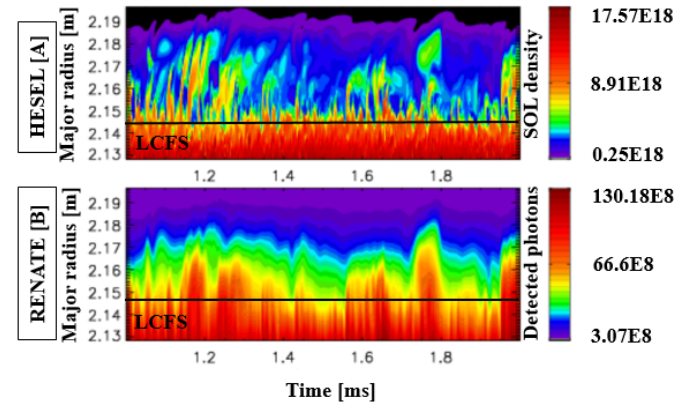


Figure 13 The time evolution of the radial density profile produced by HESEL, at the location of the diagnostic beam (A). Time evolution of radial light profile produced by synthetic BES diagnostic (B). The LCFS based on EFIT data is marked.

Based on these parameters we have performed a HESEL simulation of 3ms with the LCFS of the HESEL slab geometry being anchored to  $R = 2.145$ , the position of the LCFS is based on EFIT data. Figure 13A shows the time evolution of the radial density profile located at the centre of the beamline, featuring outwards propagating blobs of similar size, reach and frequency as shown in [33]. The time evolution of the synthetic BES signal, Figure 13B, feature light responses from fewer but larger events as the system is limited by a lower spatial resolution and smearing of the signal. The lithium beam is modelled with an FWHM diameter of 2 cm, beam energy of 50keV and beam current of 1mA. The signal is generated as an emission volume integral of the beam with direct observation volume intersection. The effective spatial source of the information extends beyond the direct observation volume, aspects of which are discussed in papers [34][35][36]. The emission smearing along the beamline, affected by the lifetime of excited  $\text{Li}_{2p}$  states, scales with the depopulation of before mentioned states by collisional processes and spontaneous emission is included by the collisional-radiative model. The flux tube expansion of HESEL density and temperature

profiles allows for the inclusion of the emission spreading caused by the line of sight to field line misalignment.

The experimental signals feature high frequencies dominated by photon noise, power spectra of SOL channels show reasonable and resembling power deposition for frequencies below 10kHz, a typical feature of SOL turbulence.

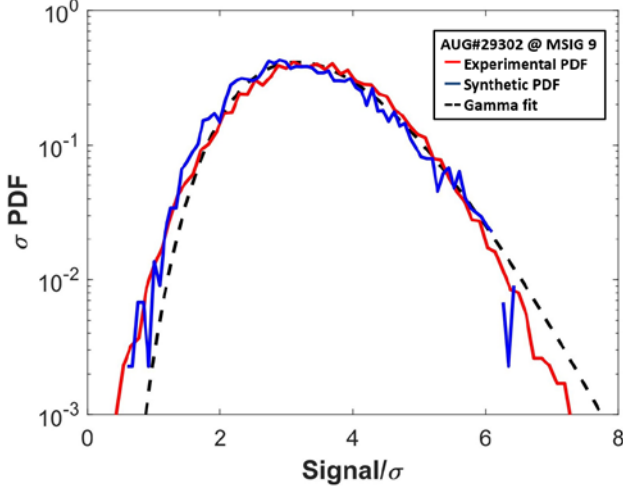


Figure 14 Probability density functions for AUG#29302 at BES channel MSIG 9, as a function of signal strength scaled by signal RMS, for experimental signal (red, solid) and synthetic signal (blue, solid). PDF-f fitted with Gamma distribution (black, dashed)

Previous work on the observation of SOL turbulence, with both probes [13][18] and BES [38] discuss the relation existing between the skewness and kurtosis of the probability density functions of measured signals and the underlying turbulence. The rescaled PDFs of experimental and synthetic AUG BES signals can be successfully fitted with Gamma functions. PDF's from channels observing the inner SOL region is shown to scale to each other, as seen in Figure 14. In the figure, we observed slightly positive skewness, indicative of the presence of blobs. This trend is observed for both synthetic and experimental signals moving towards the outer SOL region. Figure 15 shows the relationship between the skewness and kurtosis of distribution functions for both experimental and synthetic BES signals. For experimental probe signals, a parabolic relation of the form  $K = 3 + 3/S^2$  has been reported in EAST[13] and KSTAR[37] and for experimental BES signals a likewise relation has been found in KSTAR[38][39]. We note that the relationship we observed here is in close agreement with these measurements. The synthetic data (blue dots) shows a wide spread of data points on the S/K parabola, indicating the skewness of the signal increases dramatically towards the outer SOL. A region of negative skewness was found in the synthetic signals inside of the LCFS indicative of holes propagating inward. BES channels observing the plasma deeper than the numerical domain of HESEL boundary will

observe the edge information and statistics, while the beam is attenuating.

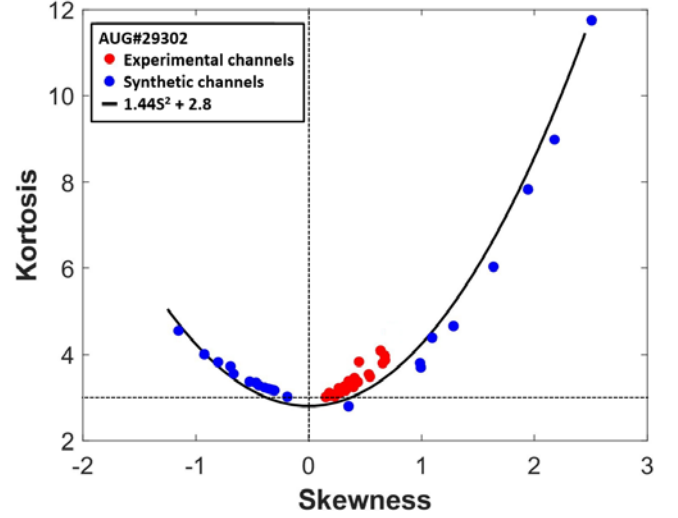


Figure 15 Kurtosis in function skewness of PDFs for experimental signals (red) and synthetic signals (blue).  $K = 1.44S^2 + 2.8$  parabola fit for the synthetic data (black).

The higher PDF moments of experimental channels (red) follow the parabolic curve, however, they are clustered in the region of low positive skewness and kurtosis close to a Gaussian distribution ( $S=0$  and  $K=3$ ), due to the amount of photonic noise characteristic of the experimental channels. No negative skewness was found in the PDFs of measured data in the edge region. This might be the result of physics that suppress the formation or lifetime of holes or the expected footprint of holes might be covered by photonic noise, making small density values undetectable. Further and more detailed investigations on this matter will be addressed in future papers.

## Discussion

Experimental observations in tokamak plasmas are by nature quite noisy and data are very frequently sparse concerning spatial and temporal resolutions. Whereas models describe the physics in terms of quantities in SI units, e.g., electron density, electron and ion temperatures and plasma potential, data from experimental observations are in currents and voltage from probes from which we extract signals such as saturation current, floating potential etc. Synthetic diagnostics, where analytical models are solved numerically and its output are converted into signals emulating a real experimental diagnostic, thus serve as important tools bridging analytical models and experiments data.

In this contribution, we have investigated SOL and edge fluctuations using synthetic diagnostics. We have demonstrated that the radial and parallel particle and energy transport in the SOL are highly intermittent. To understand the mechanism of particle and energy confinement in

tokamaks, we need to take into account the full temporal quantities and not only mean field profiles.

Based on synthetic Langmuir probe data generated using parameters from AUG#34106 we have in detail investigated fluctuations in the SOL. We have shown that analyzing experimental probe data, access to temporal electron temperature with the same sampling rate as other signals is necessary for determining the ExB drift velocity from the potential difference between two cold Langmuir probes. The influence of the electron temperature on the floating potential is too large for it to be used as a proxy for the plasma potential, for electron temperatures values relevant for MST1 experiments like AUG. Access to electron temperature fluctuations is also important deriving the electron density from the ion saturation current to a Langmuir probe, but in this case, due to the strong correlation between electron density and temperature, only the amplitudes between the signals will differ, not their frequencies.

We have also investigated the influence of the pin separation on determining the radial particle flux. As we increase this separation, there are spatial fluctuations, which the probe cannot measure and we will thus obtain smaller values of the flux. For a distance comparable to the filaments sizes, in the investigated case approximately 1-1.5 cm, we observe a drop of 50% in the measured particle flux. For a pin separation of i.e. 0.5 cm, we will measure more than 75% of the true flux.

In the SOL, synthetic probe data has been used to calculate the radial profile of the parallel heat fluxes on the outboard midplane. This profile can be mapped to the divertor to estimate the power deposition, as described in detail in [29][14]. We obtain a power law of the power fall-off length, which is in close agreement with the experimental AUG finding, see [14]. The power fall-off length is a result of both turbulent and neoclassic transport, whereas the first is normally dominating in the SOL of medium-sized tokamaks.

## References

- [1] D'Ippolito DA, Myra RA, and Zweben SJ 2011 *Phys. Plasmas* 18, 060501
- [2] Garcia OE et al 2007 *Journal of Nuclear Materials* 363-365 575-580
- [3] Naulin V 2007 *Journal of Nuclear Materials* 363-365 24-31
- [4] Nielsen AH et al 2017 *Plasma Phys. Control. Fusion* 59 025012
- [5] Tamian P et al 2016 *Journal of Computational Physics* 321 606-623
- [6] Ricci P et al 2012 *Plasma Phys. Control. Fusion* 54 124047
- [7]udson BD and Leddy J 2017 *Plasma Phys. Control. Fusion* 59 054010
- [8] Militello F et al 2016 *Plasma Phys. Control. Fusion* 58 105002
- [9] Braginskii S 1965 *Review of Plasma Physics* ed M A Leontovich vol 1 (New York, NY: Consultants Bureau) 205-311
- The turbulence is generated by the interchange dynamics, where gradients in electron and ion pressures are the driving mechanism for filamentary transport. Therefore, a natural choice of parameter for fitting the power fall-off length will be the pressure gradient across the LCFS. We have shown that we obtain a fit with the highest coefficient of determination using just two fitting parameters, the ion pressure gradient and the safety factor  $q$ . In experiments, it is, however, difficult to measure the ion pressure gradient and therefore similar investigations have not, to our knowledge, been performed.
- Finally, we have generated synthetic Li-BES signals based on a selected AUG L-mode discharge. Li-BES is a very powerful edge diagnostic for obtaining temporal density fluctuations in SOL and the edge region. The system is capable of detecting filaments in the SOL. The PDF of signals, obtained are in agreement with experimental observations from probes. For wider applications, turbulence synthetic diagnostic workflows, as the ones currently being developed within EU-IM [17], allow for the comparison of measured and synthetic turbulence dynamics in an identical frame of reference. This makes validation of turbulence codes and predictive modelling for ITER a possibility. Feasibility for the installation of ITER fluctuation BES measurements is discussed in [40][41], offering a possible tool for validation of ITER scaled turbulence models.

## Acknowledgements

This work has been carried out within the framework of the EUROfusion Consortium and has received funding from the Euratom research and training programme 2014-2018 and 2019-2020 under grant agreement No 633053. The views and opinions expressed herein do not necessarily reflect those of the European Commission.

- [10] Madsen J et al 2016 *Phys. Plasmas* 23 032306
- [11] Fundamenski W et al 2007 *Nucl. Fusion* 47 417-433
- [12] Militello F et al 2013 *Plasma Phys. Control. Fusion* 55 025005
- [13] Yan N et al 2013 *Plasma Phys. Control. Fusion* 55 115007
- [14] Olsen J et al 2018 *Plasma Phys. Control. Fusion* 60 085018
- [15] Garcia OE et al 2006 *Plasma Phys. Control. Fusion* 48 L1-L10
- [16] Imbeaux F et al 2010 *Computer Physics Communications* 181 987-998
- [17] Falchetto GL et al 2016 *Proc. 26th IAEA Fusion Energy Conference* TH/P2-13
- [18] Xu GS et al 2009 *Nucl. Fusion* 49 092002
- [19] Kube R et al 2018 *Plasma Phys. Control. Fusion* 60 065002
- [20] Graves JP et al 2005 *Plasma Phys. Control. Fusion* 47 L1
- [21] Theodorsen A et al 2016 *Plasma Phys. Control. Fusion* 58 044006
- [22] Walkden NR et al 2017 *Nucl. Fusion* 57 036016
- [23] Garcia OE et al 2017 *Physics of Plasmas* 24 032309
- [24] Garcia OE et al 2016 *Physics of Plasmas* 23, 052308

- [25] Militello F et al 2016 *Nucl. Fusion* 56 104004
- [26] Nielsen AH et al 42nd *EPS Conference on Plasma Physics*, Lisbon, Portugal 2015
- [27] Nold B et al 2012 *New Journal of Physics* 14 063022
- [28] Scott BD 2006 *Contrib. Plasma Phys.* 47, 714
- [29] Sieglin B et al 2016 *Plasma Phys. Control. Fusion* 58 055015
- [30] Zoletnik S et al 2018 *Review Sci. Instrum.* 89 063503
- [31] Guszejnov D et al 2012 *Rev. Sci. Instrum.* 83 113501
- [32] Willensdorfer M et al 2014 *Plasma Phys. Control. Fusion* 56 025008
- [33] Birkenmeier G et al 2014 *Plasma Phys. Control. Fusion* 56 075019
- [34] Asztalos O et al 2017 *EPS Plasma Physics Conference* P4.109
- [35] Ghim YC et al 2012 *Rev. Sci. Instrum.* 81 10D713
- [36] Fox MJ et al 2017 *Plasma Phys. Control. Fusion* 59 044008
- [37] Garcia OE et al 2016 *Nuclear Material and Energy* 11 008
- [38] Lampert M et al 2018 *Phys. Plasmas* 25 042507
- [39] Buzas A et al 2018 *EPS Plasma Physics Conference* P2.1091
- [40] Pokol GI et al 2013 *Fusion Eng. Des.* 88 1386
- [41] Asztalos O et al 2018 *Symposium on Fusion Technology* P4.1014